PROCEEDINGS OF SPIE

The Origins Survey Spectrometer (OSS): a far-IR discovery machine for the Origins Space Telescope

C. Matt Bradford, Bruce Cameron, Bradley Moore, Edward Amatucci, Damon Bradley, et al.

SPIE.

The Origins Survey Spectrometer (OSS): a far-IR discovery machine for the Origins Space Telescope

C. Matt Bradford[a], Bruce Cameron[a], Bradley Moore[a], Edward Amatucci[b], Damon Bradley[b], James Corsetti[b], David Leisawitz[b], S. Harvey Moseley[b], Johannes Staguhn[b], James Tuttle[b], Ari Brown[b], Alexandra Pope[c], Lee Armus[d], Margaret Meixner[e], and Klaus Pontoppidan[e]

[a]Jet Propulsion Laboratory, California Institute of Technology, Pasadena, CA, USA
[b]NASA Goddard Space Flight Center, Greenbelt, MD, USA
[c]University of Massachusetts, Amherst, MA, USA
[d]IPAC, Caltech, Pasadena, CA, USA
[e]Space Telescope Science Institute, Baltimore, MD, USA

ABSTRACT

The OSS on the Origins Space Telescope is designed to decode the cosmic history of nucleosynthesis, star formation, and supermassive black hole growth with wide-area spatial-spectral 3-D surveys across the full 25 to 590 micron band. Six wideband grating modules combine to cover the full band at R=300, each couples a long slit with 60–190 beams on the sky. OSS will have a total of 120,000 background-limited detector pixels in the six 2-D arrays which provide spatial and spectral coverage. The suite of grating modules can be used for pointed observations of targets of interest, and are particularly powerful for 3-D spectral spectral surveys. To chart the transition from interstellar material, particularly water, to planetary systems, two high-spectral-resolution modes are included. The first incorporates a Fourier-transform spectrometer (FTS) in front of the gratings providing resolving power of 25,000 ($\delta v = 12$ km/s) at $179\,\mu m$ to resolve water emission in protoplanetary disk spectra. The second boosts the FTS capability with an additional etalon (Fabry-Perot interferometer) to provide 2 km/s resolution in this line to enable detailed structural studies of disks in the various water and HD lines. Optical, thermal, and mechanical designs are presented, and the system approach to the detector readout enabling the large formats is described.

Keywords: Manuscript format, template, SPIE Proceedings, LaTeX

1. INTRODUCTION

The far-infrared, loosely defined for present purposes as the waveband between $25\,\mu m$ and $600\,\mu m$, offers a unique view of the cosmos with powerful diagnostic tools addressing a range of topics in modern astrophysics from the onset of the earliest galaxies to the formation of habitable worlds. The far-IR has lagged the optical / near-IR and radio in terms of reaching its natural performance limits because reaching these limits requires an actively-cooled space telescope and sophisticated detector technology which is not supported with military or commercial investments. The far-IR still has massive untapped scientific discovery potential available with straightforward, low-risk mission implementation. Given the progress in detector sensitivity and readout capability in the last 2 decades, we are now in a position to bring far-IR tools to bear on the most challenging problems including Universe's earliest heavy elements and the elusive late-stage gas-poor phases of planet formation.

Recognizing this opportunity, ESA, JAXA, NASA, and even Roscosmos, the Russian Space Agency, are studying approaches to cryogenic far-IR-optimized space telescopes that could be realized in the next decade and beyond. Concepts include SPICA (Roelfsema et al., this conference), the Galaxy Evolution Probe (Glenn et al., this conference), and Millimetron (Golubev et al., this conference). NASA is undertaking a study of a flagship-class far-IR facility, the Origins Space Telescope (OST), which is described in multiple papers in this conference. OST a 6-meter-class actively-cooled telescope optimized for mid- and far-IR wavelengths. Here we

---

Further author information: (Send correspondence to C.M.B.)
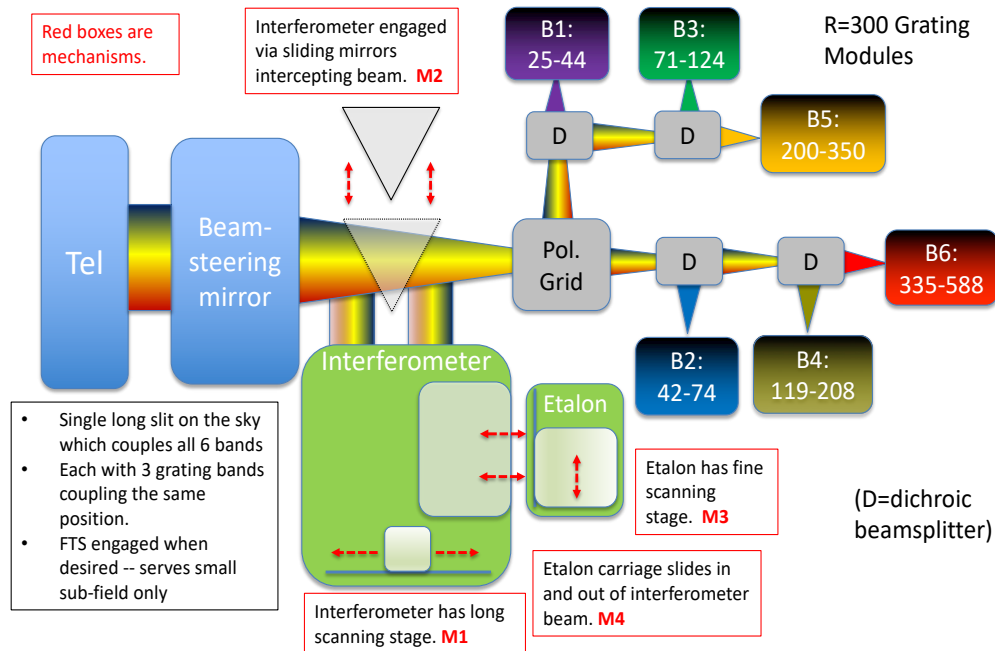C.M.B.: E-mail: matt.bradford@jpl.nasa.gov, Telephone: 1 818 726 8622

Figure 1. OSS Optical Block diagram. The 6 grating modules with their integrated detector arrays, the polarizing grid, and dichroic filters are all fixed with no mechanisms. An interferometer is inserted into the train for a small sub-field with a sliding mechanism with two mirrors on it. The interferometer is primarily a Martin Puplett polarizing Fourier-Transform system with an 8× path multiplier. In addition, the baseline design incorporates an etalon (Fabry-Perot Interferometer) which can be brought into the interferometer beam to enable very high resolution for doppler tomography experiments.

focus on the workhorse spectrograph, the Origins Survey Spectrograph (OSS), which capitalizes on large-format high-sensitivity coming detector arrays that are now within reach in the far-IR.

2. SCIENTIFIC MOTIVATION FOR WIDEBAND FAR-IR SPECTROSCOPY

A number of high priority OST scientific investigations require sensitive, wide-bandwidth spectroscopy covering the full the far-IR. The extragalactic science cases, in particular, center around charting the cosmic history of the contents and processes within galaxies from the first billion years to the present day using rest-frame mid- and far-IR spectral tracers. The various mid-IR and far-IR features originate from a wide range of interstellar medium phases: ionized, neutral atomic and molecular material, and in aggregate they constrain heavy element contents, local UV field conditions which reveal stellar properties, and physical conditions (temperature and density).[1–3] Crucially, the features in this waveband are largely immune to dust obscuration. As a group, they thus provide an unbiased census of the interplay between stars, black holes, and the interstellar material in any given observation. Of particular interest, and driving the sensitivity, is the epoch of reionization and the dawn of galaxies first billion years. As the Universe was enriched from primordial H_2 to a medium which contains heavy elements and dust grains, the key cooling pathways shifted from the quadrupole pure rotational H_2 lines (28, 17, 12, 9.7, 8.0, 6.9... μm) (e.g.[4,5]). to a combination of atomic fine-structure transitions and dust thermal emission. OST will probe all phases of this transition out to $z \sim 8 - 10$ using H_2 lines, fine-structure lines, and polycyclic aromatic hydrocarbon (PAH) features at 6.2–17 μm which have 15× more power than the brightest atomic cooling lines.[6] Both the H_2 lines and the PAH features are redshifted out of the JWST band, but not into the ALMA windows in the z ∼5–10 era. OST with the OSS spectrograph can detect these powerful bands at early epochs (Fig. 2), thus probing the transition from primordial H_2 to heavy-element cooling in the Universe's first Gyr.

Measuring these features does not require high spectral resolution, as integrated line fluxes are all that is

required. However, accessing the full time history from the first billion years to the present day does require both exquisite sensitivity (because of $1/d^2_{\text{Luminosity}}$ dimming) and coverage across the full far-IR (because of the wide intrinsic distribution of spectral features – approximately uniformly in $\log\lambda$ and the large range of redshifts). The extragalactic programs will employ both pointed observations of sources identified a priori (e.g. from JWST, WFIRST, ground-based mm/ submm surveys), as well as in blind spatial-spectral survey mode, so OSS requires good performance in both modes. Both modes will provide the full suite of mid- and far-IR spectral features, thus immediately encoding redshifts, star-formation rates, black hole accretion rates, and physical conditions. In the object-by-object pointed mode, the high-resolution mode is available (see below). This offers a direct measure of stellar and black-hole feedback through outflow signatures in OH, and other transitions, potentially a key ingredient in the decline of the cosmic star formation rate density over the last 8 billion years.[7] In the blind survey mode, millions of galaxies will be identified, with redshifts and physical parameters immediately encoded.[8] These requirements set the basic architecture for the OSS: a suite of $\mathcal{R}$=300 wideband long-slit grating spectrometers with detectors optimized for line flux detection and survey speed. The excellent line surface brightness sensitivity also enable 3-D intensity mapping of residual fluctuations after individual sources are extracted. These intensity maps can yield the total cosmic luminosity density — including all sources even those to faint to detect individually — in the key far-IR lines, charting aggregate properties of galaxies through time.[9–15]

Similarly, understanding the formation of planetary systems requires tracking the evolution of gas mass and composition in protoplanetary disks from the early (proto-stellar) phase to the late (debris-disk) stages where most of the gas has been dispersed or absorbed into giant planets. For early-stage, optically-thick disks, the fundamental of HD at $112\,\mu$m is an excellent probe of total mass; it an optically-thin chemical analog of H2, and has only a modest temperature dependence. The challenge for studying protoplanetary disks is not so much the raw spectral line sensitivity the line fluxes from disks are typically high by comparison with those of the extragalactic targets but extracting line fluxes accurately in the face of a bright dust continuum. HD, for example, can be easily washed out by the bright disk continuum so it requires a high resolving power ($\mathcal{R}\sim$ several thousand) for reliable measurement. A complement to the HD for very late-stage gas-poor disks is the 63-micron OI transition, which carries much more gas flux per column density.

Gas mass evolution is the first step, but with OST we will also study the conditions for earth-like habitability by tracking water in disks with low-lying far-IR transitions that probe the bulk of the gas including that in the snow line. Distinguishing material interior to the snow line from material further out requires a measuring line widths with a resolving power of 25,000 at wavelengths as long as 179 microns, a key ground-state water transition. This higher-resolving-power requirements are satisfied with the addition of a Fourier-transform spectrometer (FTS) which operates in tandem with the grating spectrometer suite. Finally, in order to study the structure of disks through doppler tomography, the OSS includes a very-high-resolution mode using a etalon in concert with the FTS to provide $\delta v \sim 1 - 2\,$km/s for HD $112\,\mu$m and H_2O $179\,\mu$m.

3. OVERVIEW AND SENSITIVITY

The OSS instrument block diagram is shown in Figure 1. At the heart of the instrument are 6 wideband grating modules which combine to span the full 25–590 micron range. The 25-micron minimum wavelength is designed to provide overlap with the MISC instrument, which currently intends to use Si:As blocked-impurity-band detectors, similar to those on JWST MIRI and Spitzer MIPS and IRS. The long-wavelength limit is chosen to comfortably include the ground-state water transition for local sources, and generally complement the long-term capabilities from ground-based facilities, from which high-transmission windows are for much of the band beyond 590 microns.

The grating module have no moving parts and are intended to be bolt-and-go structures, similar to the four wideband grating modules of the Spitzer IRS.[17] In the baseline design, the 6 slits overlap on the sky so that a point source couples to all 6 bands simultaneously. The wideband echelle gratings, particularly the long-wavelength ones which require compact designs typically only have high blaze efficiency in one linear polarization, so the gratings are used in single-polarization. Light from the telescope first encounters a polarizing grid, one linear polarization is passed into one arm, one is reflected into a separate arm. One arm then feeds band 1, 3, 5 while the other arm feeds bands 2, 4, 6. This staggering approach allows high-efficiency dichroic filters to separate the bands, and allows the bands to overlap slightly in the two polarizations.
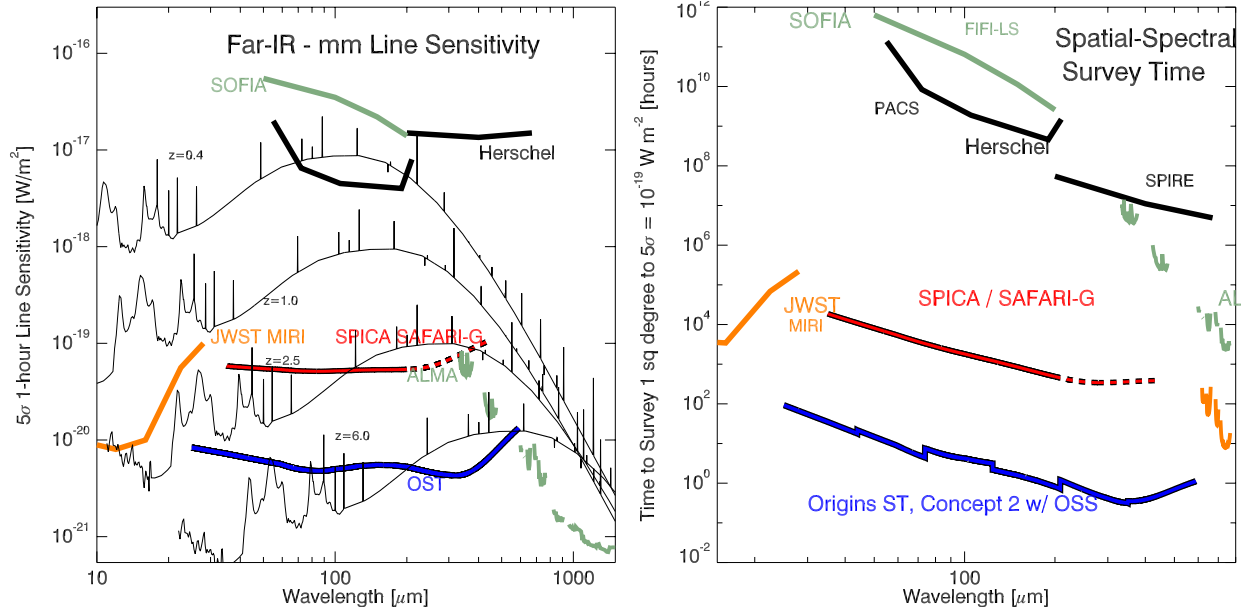
Figure 2. Spectroscopic sensitivities in the far-IR and submillimeter. Left shows the sensitivity in $W\,m^{-2}$ for a single pointed observation, assuming chopping off source to remove background (2x conservative). We use the 25 m^2 telescope area appropriate for OST concept 2. Galaxy spectra assuming $L = 10^{12}\,L_\odot$ at various redshifts are overplotted using light curves, with continuum smoothed to $\mathcal{R}=300$. The right panel shows the time required for a blind spatial-spectral survey reaching a depth of $10^{-19}\,W\,m^{-2}$ over a square degree, including the number of spatial beams and the instantaneous bandwidth (here assuming no penalty for background subtraction). The OSS instrument is the suite of $\mathcal{R}=300$ grating spectrometers with the slit lengths as designed (Table 1). Detectors are assumed to operate with NEP $= 2\times10^{-20}\,WHz^{-1/2}$, a figure which has been demonstrated in the lab. The SPICA / SAFARI-G curve refers to the new configuration: a 2.5-meter telescope with a suite of $\mathcal{R}=300$ grating spectrometer modules with 4 spatial beams, and detectors with NEP$=2\times10^{-19}\,WHz^{-1/2}$, the dashed line shows how the SPICA platform could be extended in wavelength beyond the 230 μm requirement. ALMA sensitivity refers to a $\mathcal{R}=1000$ (300 km/s) bin, and the survey speed incorporates the number of tunings of the 16 GHz total bandwidth to cover a 1:1.5 fractional band. The gold curve at lower right on the right panel shows the speed of a background-limited, wideband 100-beam spectrometer[16] on a 30-m millimeter-wave telescope at a good mountain-top site.

The grating spectrometers can be used in point-and-chop mode for deep observations of individual objects; here the observatory fine steering mirror (FSM) modulates the signal from a point source between two positions on the slit. The system can also operate as a mapping instrument in a manner similar to the Herschel SPIRE,[18] where detectors simply sample the sky as they are rastered around. For OSS on OST, this is accomplished either by using the FSM for small fields (on order the telescope FOV), or for large fields, by simply scanning the telescope itself as was done for Herschel SPIRE. Table 1 shows the high-level instrument parameters and sensitivity and mapping speed estimates for the base grating system of OSS. These are shown graphically Figure 2. As an example of the blind survey capability, consider that in Band 4, a 3000 hour map covering 3 square degrees would reach a 5σ depth of $2.6\times10^{-21}\,W\,m^{-2}$, which, for a prominent fine-structure line, corresponds to a $3.6\times10^9\,L_\odot$ galaxy at z=1, or a $1.8\times10^{11}\,L_\odot$ galaxy at z=5.

To provide higher spectral resolving power for individual sources, an interferometer can be engaged for a small field common to all bands. A sliding carriage moves two mirrors into the beam, the first diverts the beam to the interferometer optics, the second re-inserts it into the beam so that is is detected by the gratings. The interferometer is a Fourier-Transform system designed to provide 7.5 km/s resolution at 112-micron HD rotational transition; it is described more fully in Section 4.2. Using the gratings for the detection preserves the good underlying line sensitivity of the small per-detector bandwith ($\mathcal{R}=300$). Additionally, the interferometer includes an insertable etalon, which can further improve the resolving power for velocity-resolved measurements of HD and water in protoplanetary disks, this targets 1 km/s at 112 microns.

Table 1. OSS R=300 Grating Backends (on OST Concept 2 25m^2 telescope)

Parameter	Band 1	Band 2	Band 3	Band 4	Band 5	Band 6	D_{tel} sclg
λ [μm]	25–44	42–74	71–124	119–208	200–350	336–589	
Beam size [arcsec]	1.38	2.32	3.9	6.6	11.0	18.5	$\propto D^{-1}$
Slit length [arcmin]	4.65	6.5	6.5	15.6	15.6	26.7	$\propto D^{-1}$
Instantaneous FOV [sq deg]	3.1e-5	7.4e-5	1.2e-4	5.0e-4	8.5e-3	2.4e-3	$\propto D^{-2}$
Array size [mm], spectral × spatial	67×145	67×103	67×103	210×250	210×250	255×298*	
Array format spectral × spatial	168×190	168×150	168×100	168×130	168×84	168×60	
Pixel pitch [mm], spectral × spatial	0.40×0.76	0.40×0.69	0.40×1.0	1.3×1.9	1.3×2.9	1.5×3.6	
Per-beam sensitivities — includes penalty for chopping (w/ OST FSM)							
Point source line sens [W m^{-2}, 5σ, 1h]	5.4e-21	4.2e-21	4.1e-21	4.4e-21	3.5e-21	6.7e-21	$\propto D^{-2}$
Line surf bright sens [W m^{-2} sr^{-1}, 5σ, 1h]	8.4e-11	2.4e-11	8.5e-12	3.3e-12	1.0e-12	8.1e-13	$\propto D^{0}$
Point source R=4 cont. sens [μJy, 5σ, 1h]	3.2	4.1	6.8	11.9	15.9	50.	$\propto D^{-2}$
Point source mapping speeds — here perfect background subtraction is assumed							
Map. spd [deg^2/(10^{-19}W m^{-2})^2/sec]	1.9e-05	6.9e-05	1.2e-4	4.1e-4	1.0e-3	7.1e-4	$\propto D^{2}$
Map. spd [deg^2/[μJy]^2/sec]	5.2e-09	7.1e-09	4.3e-09	5.6e-09	5.1e-09	1.3e-09	$\propto D^{2}$
Pt. sce map depth, given field, given time	see example tables below						$\propto D^{-1}$
Intensity mapping sensitivity (noise. equiv. intensity / sqrt(N$_{\text{beams}}$))							
NEI /$\sqrt{\text{N}_{\text{modes}}}$ [MJy/sr/$\sqrt{\text{sec}}$], 1σ	0.24	0.13	0.094	0.050	0.034	0.046	$\propto D^{0}$

Numbers are for a 5.64-meter telescope, they can be scaled per the last column, under the assumption that the number of pixels (the optical AΩ or étendu) is fixed. Notes: Sensitivities assume single-polarization instruments with a product of cold transmission and detector efficiency of 0.25, and an aperture efficiency of 0.75. (Each beam has θ_{FWHM} of 1.13λ/D, appropriate for an assumed 10dB edge taper, and a solid angle of $\frac{\pi}{4\ln 2}\theta_{\text{FWHM}}^2$.)
* Band 6 uses two arrays with a gap between them (obscured by the grating). The total number of spatial pixels is 60, but the full 2-array system occupies the 255×298 mm footptint.
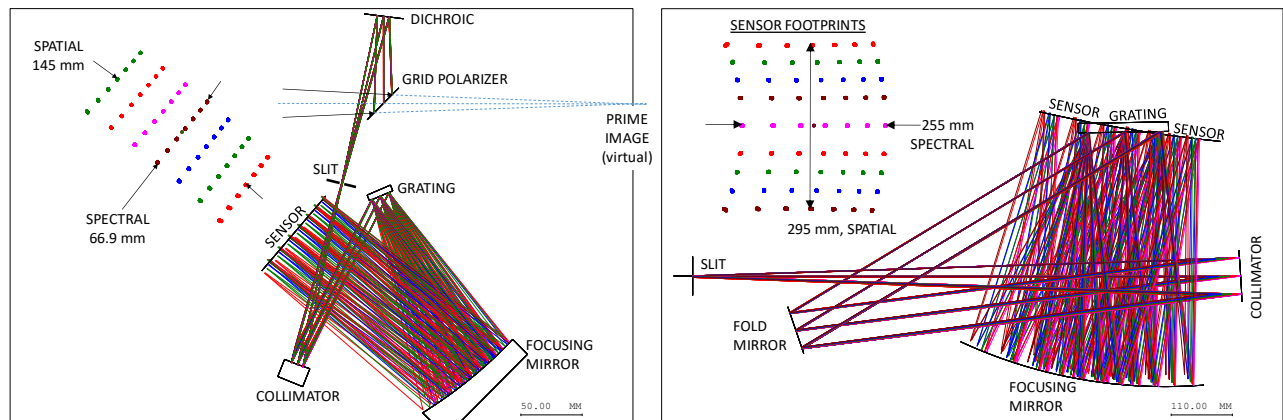
4. OPTICAL DESIGNS

Figure 3. Grating module designs for Bands 1 (left) and 6 (right), the shortest and longest-wavelength bands on OSS. In both cases the f/14.4 telescope focus is shown, this is positioned at the input slit for band 6, and conjugate to it for Band 1. Band 1 has an array longer in the spatial direction, as it images a 250-beam slit. The Band 6 focal plane uses the four spatial fields above and below the center, which is obscured by the grating. Approximately 70% of the full array footprint is used.

4.1 Grating Module Designs

The OSS design begin with the six grating spectrometer modules. These are simple, machined metal (aluminum or beryllium) structures with no moving parts. They each form a light-tight enclosure which includes the detector array, for which the only opening is a slit. Requirements provided to the optical design are:

- Slit length on sky: at least 100 diffraction-limited beams for band 1-5, and 75 beams for band 6.
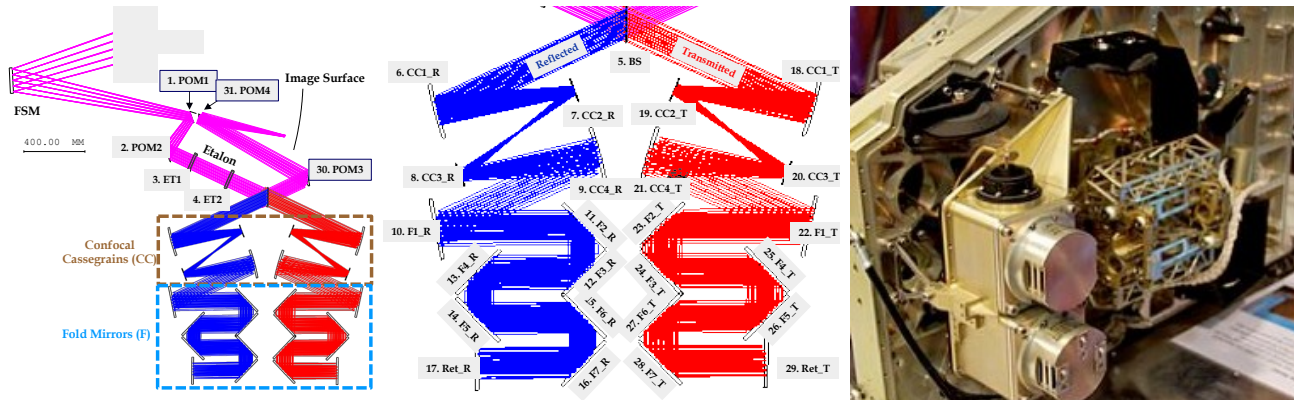
Figure 4. Optical layout for OSS interferometer. Light is intercepted in the converging beam from the telescope and collimated with a diameter of 8 cm. After processing by the interferometer, the light is re-inserted into the original light path from the telescope to the grating modules. The interferometer is engaged with a sliding stage containing POM1 and POM4; it only access a small portion of the grating slits as it it is designed primarily for single-source or small-field measurements. At right is a photograph of the Herschel SPIRE FTS, which also uses a double-sided carriage for path multiplication.

- Resolving power 300 over a 1:1.75 bandwidth.

- Strehl >80% (goal >90%) imaging to a focal plane which images a 1.15 λ/D spatial $\times$ R=300 spectral element (band-averaged) into an area no smaller than 0.25 mm^2 (to enable multiplexed detector readout, see Section 6.2).

No constraints are placed on distortion in the focal plane, or 'smile,' the non-linearity of a single spatial position's spectrum as imaged by the system, since the system has a 2-D focal plane which can be customized to the optical configuration if necessary. The size and mass of the short-wavelength gratings are driven primarily by the pixel pitch and thus array size, while the long-wavelength modules are driven by the size of the grating itself. Figure 3 shows two of the grating module designs. Notional detector array formats are tabulated for each band in Table 1, under the assumption of 1.13 fλ sampling spatially by $\mathcal{R}$=300 sampling spectrally. We emphasize that this design is not optimized, but represent a proof of concept. As is typical of wideband grating systems which use a large incidence angle the systems are highly anamorphic, with spatial f/# much faster ($\sim$2$\times$) than the spectral f/#. Optimal pixels are therefore rectangular, elongated in the spatial direction. Additionally, the physical size of an R=300 bin changes across the band, so each focal plane will have at least two spectral pitches across the full band to preserve a given fractional bandwidth per pixel – the tabulated spectral pitches are average values.

4.2 Interferometer Design

The design of the interferometer (Figure 4) is driven by the need to incorporate high spectral resolution at the long OSS wavelengths while maintaining the excellent sensitivity and multi-band capability of the base grating suite. The approach is to intercept and process the light from a small field before sending it to the grating modules for detection. This insures that the excellent sensitivity to spectral lines provided by the $\mathcal{R}=\nu/\delta\nu = 300$ detector bandwidth is preserved; the system can be considered as an extreme implementation of a band-limited FTS. When the FTS is operating (with a constant scan velocity v_{OPD}), the narrow spectral bandwidth of each grating channel corresponds to a narrow audio signal band according to the relationship

$$f_{\mathrm{audio}} = \frac{1}{\lambda_{\mathrm{optical}}\, v_{\mathrm{OPD}}}, \tag{1}$$

so each $\mathcal{R}$=300 detector need only carries signal in a narrow ($\mathcal{R}$= 300) band about the fringe rate. This provides some natural immunity against systematics and instabilities. In particular, absolute stability is not required over the full scan time.

The baseline design has a 30 cm physical throw providing 2.4 meters of optical path difference between the arms of the interferometer, providing a wavelength dependent maximum resolving power of

$$\mathcal{R}_{\text{FTS,max}} = 43,000 \times [\lambda/112\,\mu\text{m}] \tag{2}$$

which provides a good match to expected linewidths of the HD 112 μm transition in protoplanetary disks. Shorter FTS scans can be employed, which reduces $\mathcal{R}$, but the $1/\lambda$ dependence is unavoidable since the single FTS scan is common to all 6 bands. The collimated beam diameter is 8 cm, which insures that divergence (diffraction) is not a concern for the FTS operation, even at the long wavelengths. The long extra optical path between the pickoff and the interferometer retro-reflectors necessitates a pupil re-imaging to keep the system compact, this is provided by two sets of confocal off-axis Cassegrain telescopes which image the telescope pupil to the back of the interferometer.

The FTS architecture is a Martin-Puplett polarizing Fourier-transform spectrometer (FTS),[19,20] which is optimal for this application. Relative to other approaches to FTSs, this system uses a single input and single output port. It requires a linearly-polarized detector but both polarizations can be used with independent detectors. In each polarization it has unit efficiency unlike a Michelson architecture, which has power shared between the two ports.

In addition to the FTS, a second higher-res capability is designed to enable line-profile doppler tomography measurements of HD and H_2O lines in the 100–200 μm range (operation at other wavebands may be possible but is not required). This is provided with an etalon (Fabry-Perot interferometer) consisting of a 26-cm long cavity formed by two partially-reflecting mirrors which can be inserted into the beam before the FTS beam splitter. With a design finesse of 70, the etalon provides a resolving power of 325,000 (0.9 km/s) at 112 μm, or 200,000 (1.5 km/s) at 179 μm. The etalon uses the same 8 cm collimated beam provided for the FTS, but to allow for beam walk in the etalon without substantial signal loss, the mirrors must be 14 cm in diameter (and the mirrors in the FTS are similarly oversized). Once in the optical train, the cavity spacing can be changed by ∼1 mm, which provides a wavelength scan of a few orders, ample to provide complete coverage. The order number will be several thousand, so multiple orders will be coupled simultaneously to a single $\mathcal{R}$=300 grating channel. The FTS will therefore be required to sort these orders, and each step in a high-res etalon spectrum will require an order-sorting FTS scan.

4.3 Full Optical Configuration

Since all six grating modules must be fed at their slits at the telescope focus, and the slits overlap, packaging is an important consideration, and the solution has been obtained through careful iteration with the observatory mechanical and optical designs. Figure 5 shows views of the full configuration with all grating bands and the interferometer, as well as the field of view of the OSS in the

5. THERMAL DESIGN

The interferometer optics operate at the native observatory-provided 4 K, but the grating bands as well as the band separation elements (polarizing grid and dichroic filters) are all cooled further to insure that they do not impact sensitivity. We require that the potentially lossy grid and dichroic filters before the grating slits must be cooled to below the microwave background temperature to insure that they do not add background. The gratings themselves need to be below 1 K (at least at the long wavelengths) to insure that the integrated power through the bandpass filter with the full native detector étendu (AΩ) does degrade saturate the detector or degrade the noise equivalent power. These requirements are met with a continuous adiabatic demagnetization refrigerator (CADR) which stages from the observatory-provided 4 K system. The CADR is adapted from the high-heritage designs of the GSFC cooler group;[21–23] it uses 7 salt pills to provide 3 continuously-cooled stages: at 1.5 K (for the polarizing grid and dichroic filters), 0.7 K (for the grating spectrometer enclosures), and 0.05 K (for the focal plane arrays themselves).

Table 2 summarizes the calculated heat load and available lift with the cooler for each of these stages. A key advantage of the ADR approach is the high Carnot efficiency, and the CADR heat rejection is a negligible term in the 4 K budget even though it is designed to provide 100% lift margin at all of its actively cooled stages.

The 4 K situation is more challenging relative to our adopted allocation from the observatory, and remains an area of study. 4 K houses the first stage low-noise amplifier, and the 0.5 mW in the table corresponds to commercially-available amplifiers operating up to 8 GHz, but we expect that improvements in amplifier power dissipation should be possible. Of course, a straightforward descope to ease this aspect is to simply not operate all 6 bands simultaneously. (Parasitic conduction in harnesses are book-kept at observatory level, but are much smaller than the amplifier dissipation.)

6. DETECTOR AND READOUT APPROACH

Detectors which are capable of taking advantage of the low-background space environment must be substantially more sensitive than any that have been used scientifically to date (Figure 7), and beyond what is required for even the most extreme instruments in ground-based or sub-orbital platforms. Furthermore, the OSS has a total of 120,000 pixels in the 6 arrays, a factor of ∼30 more than was fielded in Herschel. Fortunately, the sensitivity and format are separable problems, and in the last few years, solutions to both the sensitivity and format have been demonstrated in the laboratory. Unlike the near-IR and mid-IR detector arrays, detectors for OSS and the
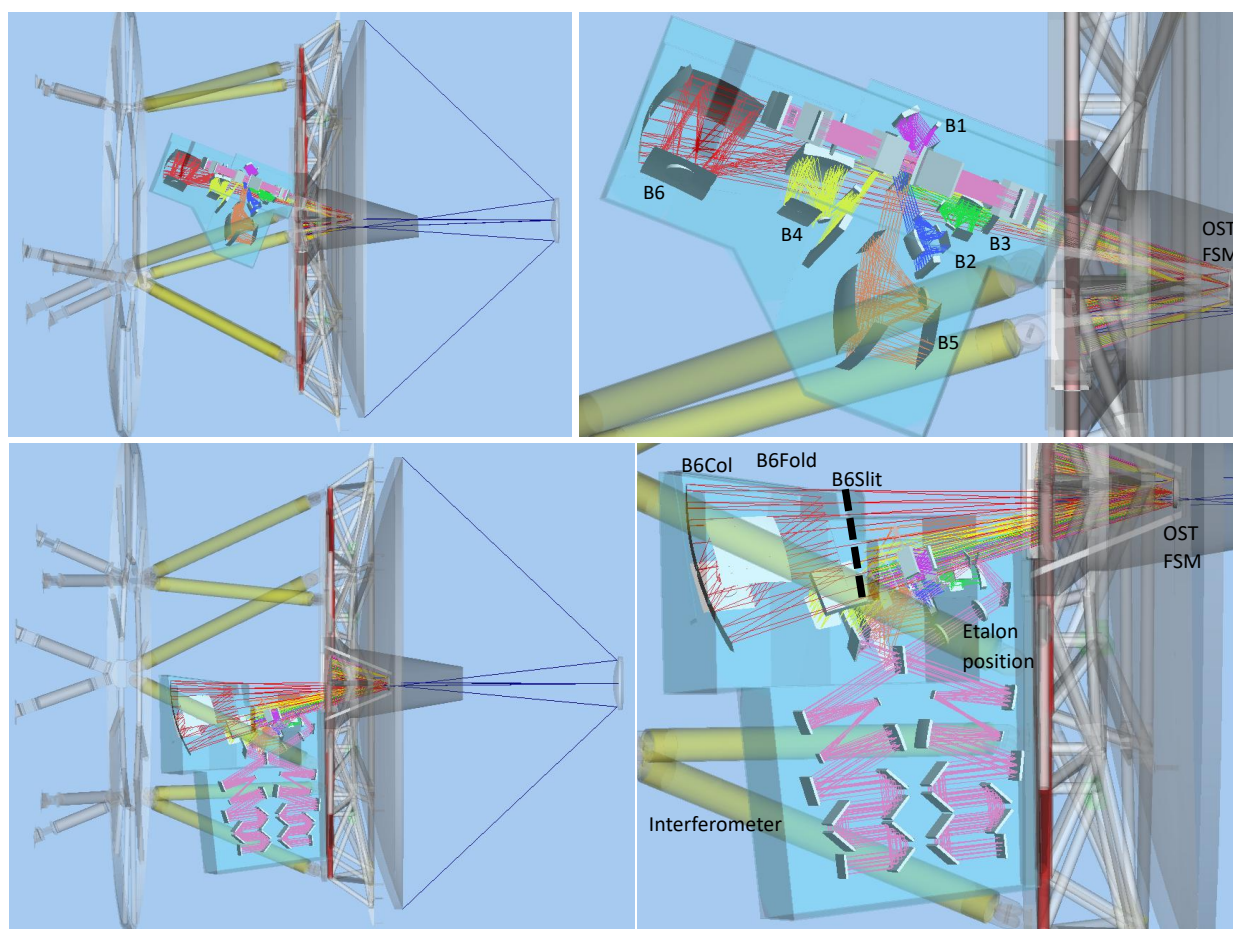

Figure 5. Configuration of the OSS with the OST telescope. Right-hand panels are zoomed views of left hand panels. Grating modules are arrayed in a plane which is approximately orthogonal to the plane of the interferometer bench, so two views are provided with the telescope, they differ by a rotation about the telescope boresight. Top shows the shows the 6 grating spectrometer bands, with notional enclosure. A polarizing grid picks off on polarization and sends it down to illuminate bands 1, 3 and 5. Bands 2, 4, 6 couple to the transmitted beam via reflective dichroic filters. The entrance to band 6 is the natural telescope focus position. Bottom shows the interferometer bench and the full extent of the band 6 collimator.
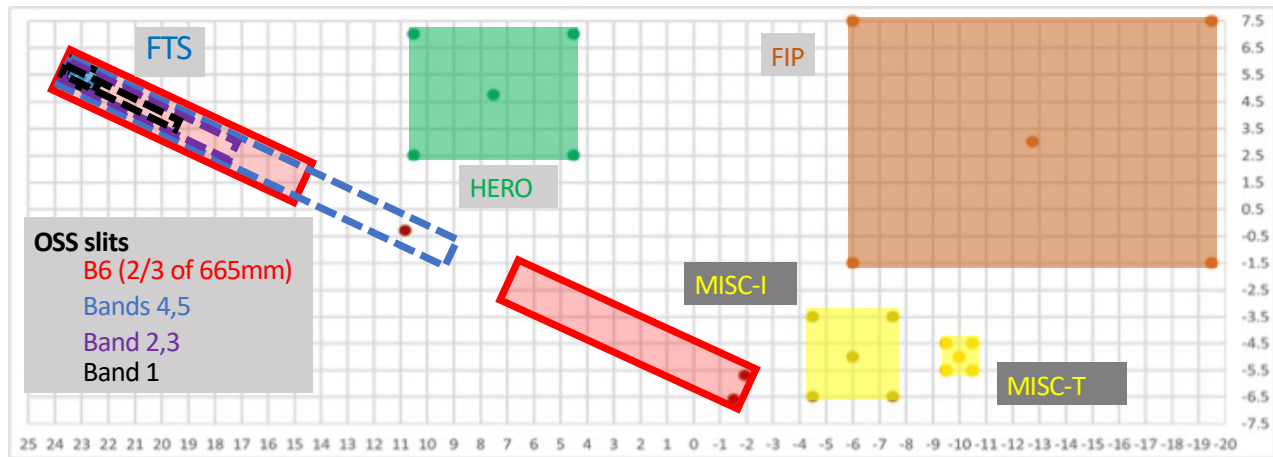
Figure 6. OST field of view, units are arcminutes. The various OSS slits (widths not to scale) overlap in the upper left, and the ~1.5 arcminute interferometer field is at the upper left end of the slits.

Table 2. OSS Thermal Loads and Heat Lifts of Cryogenic Stages

Source	Load [μW]	
50 mK stage total	2.94	
Conduction from NbTi coaxial lines (126) 1 meter from 0.7 K		0.247
Conduction in Ti 15-3-3-3 struts from 0.7 K (total A/L = 1.22 mm)		1.35
Conduction in thermometer leads		negligible
Dissipation in detectors (10.3 pW × 130k pixels) (TES MUX)		1.34
Design Lift of 50 mK stage	6	
0.7 K stage total	107	
Conduction from NbTi coaxial lines (126 at 1 m from 1.6 K)		2.6
Conduction in Ti 15-3-3-3 struts from 1.6 K (total A/L = 1.22 mm)		104
Conduction in thermometer leads		negligible
Design Lift of 0.7 K stage	292	
1.6 K stage total	2110	
Conduction in supports for band separation optics		960
Conduction in NbTi coaxial lines (126 at 1 m from 4.0 K)		36
Conduction from 4 K in Ti 15-3-3-3 struts supporting grating modules		1110
Design Lift of 1.5 K stage	4250	
4 K stage total	49,000	
From ADR operation (average, at full design values)		11,000
FTS Mechanism		4,000
Amplifiers at 4 K (68 × 0.5 mW)		34,000
OST provided allocation for OSS	42,000	

other sensitive far-IR instrumentation must being developed by science-driven teams, many of which are centered at NASA and some of the national agencies in Europe and Japan, and most of which include collaboration with university groups. Many papers are presented on these devices in the 'Millimeter-Wave Detectors' portion of this conference and at the Low-Temperature Detectors conferences. Here we outline how these technologies are implemented in a system design for the OSS instrument and the OST mission. *We emphasize that a modest but sustained NASA-supported effort in far-IR detectors is important for enabling the OST and other far-IR missions under consideration.*

Before describing the detector approaches, we also note for completeness the other important detector requirements, none of which pose particular challenges compared with the sensitivity and scaling up to the desired
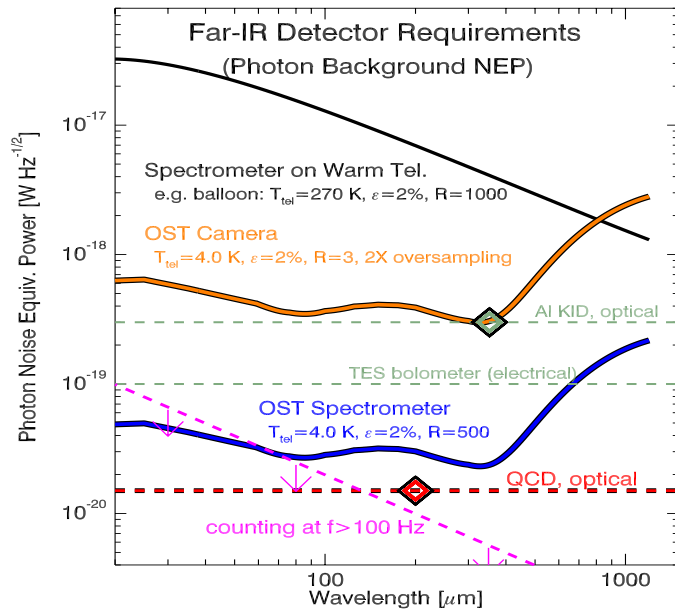
Figure 7. Sensitivity (noise equivalent power – NEP) requirements for far-IR instrumentation on various platforms. Curves show the photon shot noise, improving detectors beyond this produces diminishing gains. The most demanding platform is the OST spectrometer (OSS), for which the photon NEP is as low as $4\times10^{-19}\,\mathrm{W\,Hz^{-1/2}}$. Horizontal lines show published measurements, the aluminum KID is from the SRON group,[?] TES bolometers at $1\times10^{-19}\,\mathrm{W\,Hz{-1/2}}$ have been measured at both JPL and SRON.[24,25] The QCD is described in Echternach et al (2018).[26] If devices become sufficiently sensitive, and have enough speed, they can count photons, as has been demonstrated with the QCD.

format. The devices must be sufficiently fast to enable scan mapping at the short wavelengths, and a similar speed requirement exists for using the FTS at the short wavelengths per Equation 1. They must be responsive at 150 Hz, corresponding to a speed of response (time constant) of 1 ms. They must also have sufficient dynamic range to permit observations of Galactic sources at their photon noise limit. With the 25-m^2 telescope, a 1 Jy source at 80 μm, presents $\sim$500$\times$ the flux on a detector as the zodical background.

6.1 Detector Approaches

In order of technical readiness the detector candidates from which the OSS will downselect are:

- Superconducting transition-edge-sensed (TES) bolometers, which have been used in a variety of ground[27–30] and sub-orbital platforms.[31] For OSS, the key virtue of the TES system is the high heritage, along with the demonstrated NEPs as low as $1\times10^{-19}\,\mathrm{W\,Hz^{-1/2}}$ at both JPL and SRON.[25,32] Pushing to lower NEPs is possible, though potentially cumbersome: either base temperatures must be reduced from the canonical 50 mK, and/or the leg isolation needs to be improved with more exotic micro-fabricated structures. A principal disadvantage of TES systems, particularly for the formats required for OSS is the complexity of focal plane assembly for TES systems, in particular the hybridization with superconducting quantum interference devices (SQUIDs), typically one per detector.

- Kinetic inductance detectors (KIDs) offer a much simpler implementation by combining the detection with the readout resonator, so that in many cases KID arrays can be implemented with 1 or 2 thin film metal layers simply patterned on silicon. KIDs have progressed rapidly since their inception in 2003.[33] They have been and are in use in several ground-based experiments,[34–39] and are now being prepared for the BLAST-Pol2 balloon experiment.[40] The best reported KID sensitivities are now $3\times10^{-19}\,\mathrm{W\,Hz^{-1/2}}$ (a figure that far exceeds the requirements for ground-based or suborbital work), and this has been demonstrated in at the kilo-pixel formats with good yield and uniformity.[41] The principal challenge for KIDs is to bring down the NEP a factor of 10 to the OSS levels. The most straightforward path to lower NEP is to reduce the device volume, while maintaining a reasonable resonant frequency and a design which can efficiently absorb photons. Scaling arguments based on the existing measurements suggest that factors of at least 3 and perhaps more reduction in NEP relative to the state of the art should be obtainable, but this has yet to be demonstrated.

- The quantum capacitance detector (QCDs) is an emerging technology which has demonstrated excellent sensitivity and even individual photon counting in the far-IR.[26,42] As with a KID, the incident photons
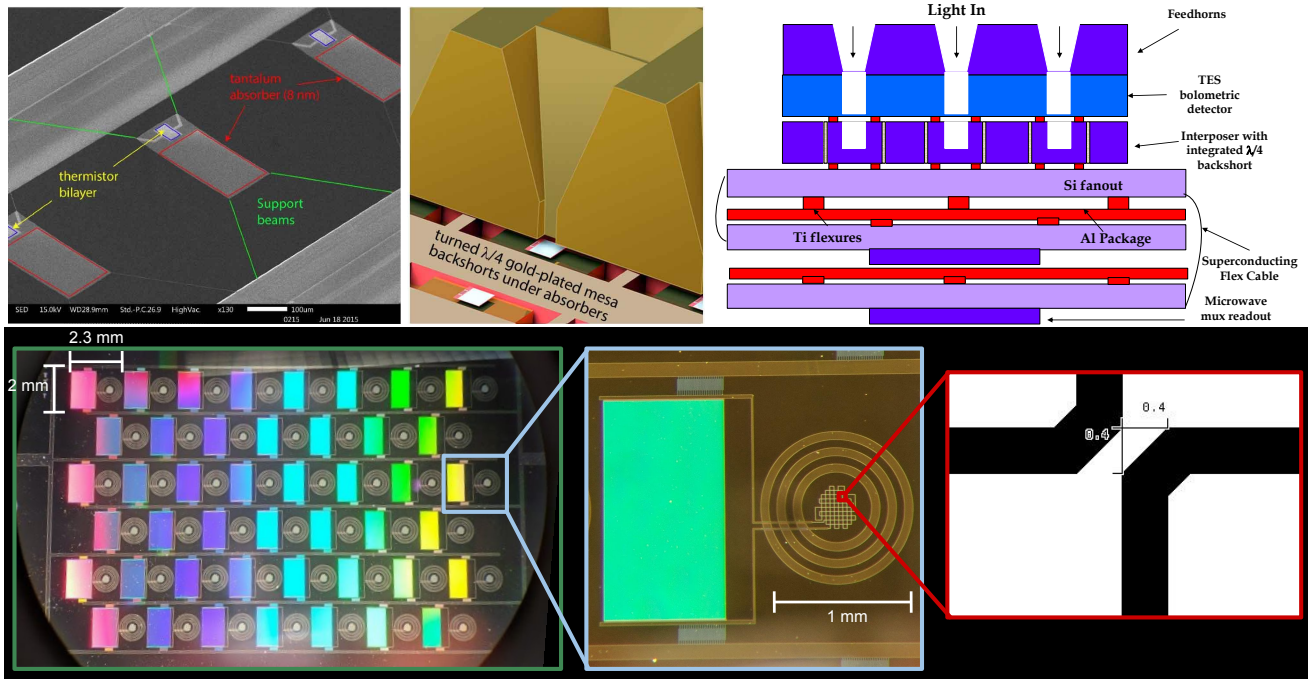
Figure 8. Examples of OSS detector approaches. The top panels show transition-edge sensed (TES) bolometers. At left is a zoom in of bolometer built at SRON which has demonstrated $1\times10^{-19}\,\mathrm{W\,Hz^{-1/2}}$ and good speed of response. Center shows a feedhorn + backshort schematic which provides good coupling to the the absorbers. (horns will be close-packed for OSS). Right shows the schematic of the stackup that enables the hybridization with the microwave multiplexer for the TES bolometers. Bottom montage shows a prototype kinetic-inductance detector (KID) array built in the JPL microdevices lab (MDL) (photo montage credit: Alyssa Barlis). The entire array, including the readout lines, is patterned in a single 40 nm layer of aluminum patterned directly on silicon. These devices are absorb photons in both polarizations directly in the meandered inductor at the center of the device; they are coupled with feedhorns, but micro-lenses may also work. This prototype has demonstrated high yield and noise equivalent power (NEP) of $4\times10^{-18}\,\mathrm{W\,Hz^{-1/2}}$.[43] Much lower NEP should be possible with this architecture, scaling from the high-sensitivity, large-volume devices developed at SRON.[41]

break Cooper pairs and establish a density of quasiparticles (free electrons) in a superconducting absorber. The QCD, however, detects quasiparticles (free electrons) tunneling from a superconducting absorber which is separate from the resonator, so it offers an additional degree of freedom in the design. Single tunneling events change the capacitance of the resonator enough to shift the frequency by a large fraction of a linewidth, so individual tunneling is detectable. A single far-IR photon produces several quasiparticles, each of which tunnels many times, so the system can easily provide shot-noise-limited performance and even photon counting down to very lower power levels. The QCD is an exciting development, particularly given the relatively modest investment to date, but much remains to be shown. The tunnel junctions are particularly challenging, even a modest array with useful yield and stability remains to be demonstrated.

6.2 Readout with Superconducting Micro-Resonators

For all of the detector systems being considered, the large array formats for OSS are enabled by superconducting high quality factor (Q) micro-resonators operating in the RF or microwave, an approach pioneered with the kinetic inductance detector.[33, 44] With individual resonator Qs of 10^5, $\sim10^3$–10^4 resonators can be arrayed in an octave of readout frequency band, and all accessed with a single readout line. Resonator frequencies as low as 50 MHz and as high as 10 GHz have been used in various far-IR detector demonstrations. The resonators are patterned lithographically in superconducting thin films such as aluminum, niobium or titanium nitride; they can be either transmission line segments, or lumped-element (LC) devices. An important system-level consideration
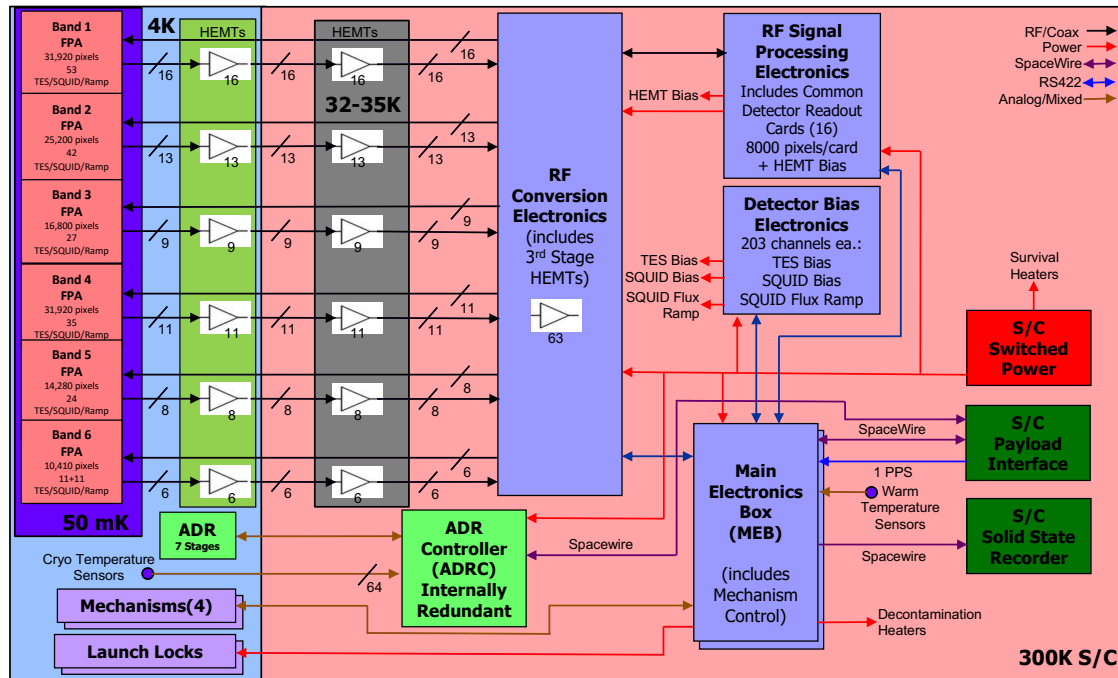
Figure 9. OSS Electrical block diagram. The detector readout consists 63 circuits each carrying 4 GHz of information bandwidth. Detectors are coupled to micro-resonators, 2000 can be read out in each line. On the warm spacecraft side, electronics both create the waveform that interacts with the array, and then digitizes and analyzes the return waveform to extract phase shifts which encode detector signals.

is the per-resonator area, as this sets the pixel pitch for the simplest architectures in which the detectors and resonators are patterned together on the same silicon wafer. This area scales typically a $1/f_{res}^2$. On the other hand the power dissipation in the warm electronics scales as f_{max}, so this choice involves a system-level trade.

For the OSS point design, we have adopted a conservative readout system approach that can accommodate any of the detector approaches. We baseline resonator frequencies of 4–8 GHz, and a resonator spacing of 2 MHz. Each readout circuit therefore can process 2,000 pixels, and when partitioned into integer readout circuits for the six arrays, the total number of circuits required for all six is 63. The hard work is done in dedicated electronics on the warm spacecraft side. Each circuit generates a frequency comb containing the 2000 tones, this is delivered to the cold stage with a coaxial line, attenuated along the way at the various cold stages. This comb interacts with the array, each detector introducing a unique phase shift according to its optical signal, and the returning signal is amplified and delivered back to the warm side via another coaxial line. The signal is first converted to the -2 GHz to 2 GHz baseband, then digitized in chunks corresponding to the scientific sampling interval (e.g. 250 micro-seconds interval with 1 million samples at 4 Gs/s). Each chunk is then processed with dedicated digital spectrometer logic to extract the phase shift of each tone with respect to the input, this encodes the optical signal for that scientific sample.

Examples of such readout systems which have been demonstrated on sky include a early FPGA-based systems for KIDs at UCSB,[45] and Caltech,[37] these have evolved into the current generation using ROACH-2 hardware, a prime example is that developed at ASU.[46] In parallel, a microwave readout has been developed for TES bolometers using SQUIDs combined with microwave resonators,.[47,48] These systems have very similar, nearly interchangeable, warm electronics*.

The total warm electronics power dissipation is the principal system-level concern. It scales as the maximum baseband frequency (equal to the total frequency range if mixing up), 2 GHz for our baseline OSS design. Both

---

*The TES system still requires a DC detector bias run independently of the readout, and a discrete SQUID for each detector, so it is a more complicated implementation at the focal plane, an aspect which has been included in our study.

the analog-to-digital conversion (ADC) and digital signal processing, as well as their interfacing can be power intensive depending on the implementation. The existing FPGA-based readout for KIDs, which has had no optimization for power consumption, processes a single circuit with frequencies up to 500 MHz and requires about 50 W. However, massive gains now available. A particular example is the new Xilnix RF-system on chip (SoC) which integrates the ADC with programmable digital signal processing logic (FPGA-like) in a single chip based on 16-nm-gate CMOS transistors. A single chip provides eight channels, each capable of processing 2 GHz at 12 bits depth, and the associated waveform generation capability, it represents approximately 8 x (2 / 0.5) = 32 times the processing capability the fiducial existing FPGA-based readout. A board with this chip is being released by Abaco as of this writing [†], initial power dissipation estimates from are 50 W for this board at full utilization. Our system design uses this power dissipation fiducial of 50 W per 16 GHz of information bandwidth for the ADC and digital spectrometer logic. We consider this a conservative estimate – while neither of these existing systems are flight-qualified, mixed-signal application-specific integrated circuits (ASICs) which integrate ADCs and signal processing have been developed for flight implementation of similar applications, [49,50] and these systems typically have lower power dissipation than their programmable-logic counterparts,

ACKNOWLEDGMENTS

REFERENCES

[1] Stacey, G. J., "Far-Infrared Spectroscopy Diagnostics of the Interstellar Medium in Galaxies," in [*Astronomical Infrared Spectroscopy: Future Observational Directions*], Kwok, S., ed., *Astronomical Society of the Pacific Conference Series* **41**, 297 (Jan. 1993).

[2] Colbert, J. W., Malkan, M. A., Clegg, P. E., Cox, P., Fischer, J., Lord, S. D., Luhman, M., Satyapal, S., Smith, H. A., Spinoglio, L., Stacey, G., and Unger, S. J., "ISO LWS Spectroscopy of M82: A Unified Evolutionary Model," *ApJ* **511**, 721–729 (Feb. 1999).

[3] Dale, D. A., Smith, J. D. T., Schlawin, E. A., Armus, L., Buckalew, B. A., Cohen, S. A., Helou, G., Jarrett, T. H., Johnson, L. C., Moustakas, J., Murphy, E. J., Roussel, H., Sheth, K., Staudaher, S., Bot, C., Calzetti, D., Engelbracht, C. W., Gordon, K. D., Hollenbach, D. J., Kennicutt, R. C., and Malhotra, S., "The Spitzer Infrared Nearby Galaxies Survey: A High-Resolution Spectroscopy Anthology," *ApJ* **693**, 1821–1834 (Mar. 2009).

[4] Ogle, P., Davies, J. E., Appleton, P. N., Bertincourt, B., Seymour, N., and Helou, G., "Ultraluminous Star-forming Galaxies and Extremely Luminous Warm Molecular Hydrogen Emission at z = 2.16 in the PKS 1138-26 Radio Galaxy Protocluster," *ApJ* **751**, 13 (May 2012).

[5] Ogle, P., Boulanger, F., Guillard, P., Evans, D. A., Antonucci, R., Appleton, P. N., Nesvadba, N., and Leipski, C., "Jet-powered Molecular Hydrogen Emission from Radio Galaxies," *ApJ* **724**, 1193–1217 (Dec. 2010).

[6] Smith, J. D. T., Draine, B. T., Dale, D. A., Moustakas, J., Kennicutt, Jr., R. C., Helou, G., Armus, L., Roussel, H., Sheth, K., Bendo, G. J., Buckalew, B. A., Calzetti, D., Engelbracht, C. W., Gordon, K. D., Hollenbach, D. J., Li, A., Malhotra, S., Murphy, E. J., and Walter, F., "The Mid-Infrared Spectrum of Star-forming Galaxies: Global Properties of Polycyclic Aromatic Hydrocarbon Emission," *ApJ* **656**, 770–791 (Feb. 2007).

[7] Armus, L., Bolatto, A., Pope, A., Bradford, C. M., and Origins Space Telescope Science and Technology Definition Team, "Measuring Galactic Feedback with the Origins Space Telescope," in [*American Astronomical Society Meeting Abstracts #231*], *American Astronomical Society Meeting Abstracts* **231**, 355.05 (Jan. 2018).

[†]`https://www.abaco.com/products/vp430-rfsoc-board`

[8] Pope, A., Armus, L., bradford, c., and Origins Space Telescope STDT, "Origins Space Telescope: 3D infrared surveys of star formation and black hole growth in galaxies over cosmic time," in [*American Astronomical Society Meeting Abstracts #231*], *American Astronomical Society Meeting Abstracts* **231**, 355.50 (Jan. 2018).

[9] Visbal, E. and Loeb, A., "Measuring the 3D clustering of undetected galaxies through cross correlation of their cumulative flux fluctuations from multiple spectral lines," *J. Cos. Astroparticle Phys* **11**, 16–+ (Nov. 2010).

[10] Visbal, E., Trac, H., and Loeb, A., "Demonstrating the feasibility of line intensity mapping using mock data of galaxy clustering from simulations," *J. Cos. Astroparticle Phys* **8**, 10–+ (Aug. 2011).

[11] Gong, Y., Cooray, A., Silva, M. B., Santos, M. G., and Lubin, P., "Probing Reionization with Intensity Mapping of Molecular and Fine-structure Lines," *ApJL* **728**, L46+ (Feb. 2011).

[12] Gong, Y., Cooray, A., Silva, M., Santos, M. G., Bock, J., Bradford, C. M., and Zemcov, M., "Intensity Mapping of the [C II] Fine Structure Line during the Epoch of Reionization," *ApJ* **745**, 49 (Jan. 2012).

[13] Gong, Y., Cooray, A., and Santos, M. G., "Probing the Pre-reionization Epoch with Molecular Hydrogen Intensity Mapping," *ApJ* **768**, 130 (May 2013).

[14] Uzgil, B. D., Aguirre, J. E., Bradford, C. M., and Lidz, A., "Measuring Galaxy Clustering and the Evolution of [C II] Mean Intensity with Far-IR Line Intensity Mapping during $0.5 < z < 1.5$," *ApJ* **793**, 116 (Oct. 2014).

[15] Serra, P., Doré, O., and Lagache, G., "Dissecting the High-z Interstellar Medium through Intensity Mapping Cross-correlations," *ApJ* **833**, 153 (Dec. 2016).

[16] Bradford, C. M., Hailey-Dunsheath, S., Shirokoff, E., Hollister, M., McKenney, C. M., LeDuc, H. G., Reck, T., Chapman, S. C., Tikhomirov, A., Nikola, T., and Zmuidzinas, J., "X-Spec: a multi-object trans-millimeter-wave spectrometer for CCAT," in [*Millimeter, Submillimeter, and Far-Infrared Detectors and Instrumentation for Astronomy VII*], *Proc. of the SPIE* **9153**, 91531Y (Aug. 2014).

[17] Houck, J. R., Roellig, T. L., Van Cleve, J., Forrest, W. J., Herter, T. L., Lawrence, C. R., Matthews, K., Reitsema, H. J., Soifer, B. T., Watson, D. M., Weedman, D., Huisjen, M., Troeltzsch, J. R., Barry, D. J., Bernard-Salas, J., Blacken, C., Brandl, B. R., Charmandaris, V., Devost, D., Gull, G. E., Hall, P., Henderson, C. P., Higdon, S. J. U., Pirger, B. E., Schoenwald, J., Sloan, G. C., Uchida, K. I., Appleton, P. N., Armus, L., Burgdorf, M. J., Fajardo-Acosta, S. B., Grillmair, C. J., Ingalls, J. G., Morris, P. W., and Teplitz, H. I., "The infrared spectrograph on the Spitzer Space Telescope," in [*Optical, Infrared, and Millimeter Space Telescopes*], Mather, J. C., ed., *Proc. of the SPIE* **5487**, 62–76 (Oct. 2004).

[18] Griffin, M. J., Abergel, A., Abreu, A., Ade, P. A. R., André, P., Augueres, J., Babbedge, T., Bae, Y., Baillie, T., Baluteau, J., Barlow, M. J., Bendo, G., Benielli, D., Bock, J. J., Bonhomme, P., Brisbin, D., Brockley-Blatt, C., Caldwell, M., Cara, C., Castro-Rodriguez, N., Cerulli, R., Chanial, P., Chen, S., Clark, E., Clements, D. L., Clerc, L., Coker, J., Communal, D., Conversi, L., Cox, P., Crumb, D., Cunningham, C., Daly, F., Davis, G. R., de Antoni, P., Delderfield, J., Devin, N., di Giorgio, A., Didschuns, I., Dohlen, K., Donati, M., Dowell, A., Dowell, C. D., Duband, L., Dumaye, L., Emery, R. J., Ferlet, M., Ferrand, D., Fontignie, J., Fox, M., Franceschini, A., Frerking, M., Fulton, T., Garcia, J., Gastaud, R., Gear, W. K., Glenn, J., Goizel, A., Griffin, D. K., Grundy, T., Guest, S., Guillemet, L., Hargrave, P. C., Harwit, M., Hastings, P., Hatziminaoglou, E., Herman, M., Hinde, B., Hristov, V., Huang, M., Imhof, P., Isaak, K. J., Israelsson, U., Ivison, R. J., Jennings, D., Kiernan, B., King, K. J., Lange, A. E., Latter, W., Laurent, G., Laurent, P., Leeks, S. J., Lellouch, E., Levenson, L., Li, B., Li, J., Lilienthal, J., Lim, T., Liu, S. J., Lu, N., Madden, S., Mainetti, G., Marliani, P., McKay, D., Mercier, K., Molinari, S., Morris, H., Moseley, H., Mulder, J., Mur, M., Naylor, D. A., Nguyen, H., O'Halloran, B., Oliver, S., Olofsson, G., Olofsson, H., Orfei, R., Page, M. J., Pain, I., Panuzzo, P., Papageorgiou, A., Parks, G., Parr-Burman, P., Pearce, A., Pearson, C., Pérez-Fournon, I., Pinsard, F., Pisano, G., Podosek, J., Pohlen, M., Polehampton, E. T., Pouliquen, D., Rigopoulou, D., Rizzo, D., Roseboom, I. G., Roussel, H., Rowan-Robinson, M., Rownd, B., Saraceno, P., Sauvage, M., Savage, R., Savini, G., Sawyer, E., Scharmberg, C., Schmitt, D., Schneider, N., Schulz, B., Schwartz, A., Shafer, R., Shupe, D. L., Sibthorpe, B., Sidher, S., Smith, A., Smith, A. J., Smith, D., Spencer, L., Stobie, B., Sudiwala, R., Sukhatme, K., Surace, C., Stevens, J. A., Swinyard, B. M., Trichas, M., Tourette, T., Triou, H., Tseng, S., Tucker, C., Turner, A., Vaccari, M., Valtchanov, I., Vigroux, L., Virique, E., Voellmer, G., Walker, H., Ward, R., Waskett, T., Weilert, M., Wesson, R., White, G. J., Whitehouse, N., Wilson, C. D., Winter, B., Woodcraft, A. L., Wright, G. S., Xu, C. K., Zavagno, A., Zemcov, M., Zhang, L., and Zonca, E., "The Herschel-SPIRE instrument and its in-flight performance," *A&A* **518**, L3+ (July 2010).

[19] Martin, D. and Puplett, E., "Polarised interferometric spectrometry for the millimetre and submillimetre spectrum," *Infrared Physics* **10**(2), 105 – 109 (1970).

[20] Lambert, D. K. and Richards, P. L., "Martin-puplett interferometer: an analysis," *Appl. Opt.* **17**, 1595–1602 (May 1978).

[21] Shirron, P. J., Canavan, E. R., DiPirro, M. J., Tuttle, J. G., and Yeager, C. J., [*A Multi-Stage Continuous-Duty Adiabatic Demagnetization Refrigerator*], 1629–1638, Springer US, Boston, MA (2000).

[22] Shirron, P. J., Kimball, M. O., Wegel, D. C., Canavan, E. R., and Dipirro, M. J., "Design of a 3-stage ADR for the soft x-ray spectrometer instrument on the ASTRO-H mission," in [*Society of Photo-Optical Instrumentation Engineers (SPIE) Conference Series*], *Society of Photo-Optical Instrumentation Engineers (SPIE) Conference Series* **7732**, 12 (July 2010).

[23] Shirron, P. J., Kimball, M. O., James, B. L., Muench, T., DiPirro, M. J., Letmate, R. V., Sampson, M. A., Bialas, T. G., Sneiderman, G. A., Porter, F. S., and Kelley, R. L., "Operating modes and cooling capabilities of the 3-stage adr developed for the soft-x-ray spectrometer instrument on astro-h," *Cryogenics* **74**, 2 – 9 (2016). 2015 Space Cryogenics Workshop, June 24Ä\26, 2015, Phoenix, AZ Hosted by NASA Glenn Research Center, Cleveland, OH, USA.

[24] Beyer, A. D., Echternach, P. M., Kenyon, M. E., Runyan, M. C., Bumble, B., Bradford, C. M., Bock, J. J., and Holmes, W. A., "Effect of mo/cu superconducting bilayer geometry on ultra-sensitive transition-edge sensor performance," *IEEE Transactions on Applied Superconductivity* **23**, 2100104–2100104 (June 2013).

[25] Khosropanah, P., Suzuki, T., Ridder, M. L., Hijmering, R. A., Akamatsu, H., Gottardi, L., van der Kuur, J., Gao, J. R., and Jackson, B. D., "Ultra-low noise tes bolometer arrays for safari instrument on spica," (2016).

[26] Echternach, P. M., Pepper, B. J., Reck, T., and Bradford, C. M., "Single photon detection of 1.5 THz radiation with the quantum capacitance detector," *Nature Astronomy* **2**, 90–97 (Jan. 2018).

[27] Holland, W. S., Bintley, D., Chapin, E. L., Chrysostomou, A., Davis, G. R., Dempsey, J. T., Duncan, W. D., Fich, M., Friberg, P., Halpern, M., Irwin, K. D., Jenness, T., Kelly, B. D., MacIntosh, M. J., Robson, E. I., Scott, D., Ade, P. A. R., Atad-Ettedgui, E., Berry, D. S., Craig, S. C., Gao, X., Gibb, A. G., Hilton, G. C., Hollister, M. I., Kycia, J. B., Lunney, D. W., McGregor, H., Montgomery, D., Parkes, W., Tilanus, R. P. J., Ullom, J. N., Walther, C. A., Walton, A. J., Woodcraft, A. L., Amiri, M., Atkinson, D., Burger, B., Chuter, T., Coulson, I. M., Doriese, W. B., Dunare, C., Economou, F., Niemack, M. D., Parsons, H. A. L., Reintsema, C. D., Sibthorpe, B., Smail, I., Sudiwala, R., and Thomas, H. S., "SCUBA-2: the 10 000 pixel bolometer camera on the James Clerk Maxwell Telescope," *MNRAS* **430**, 2513–2533 (Apr. 2013).

[28] Staniszewski, Z., Aikin, R. W., Amiri, M., Benton, S. J., Bischoff, C., Bock, J. J., Bonetti, J. A., Brevik, J. A., Burger, B., Dowell, C. D., Duband, L., Filippini, J. P., Golwala, S. R., Halpern, M., Hasselfield, M., Hilton, G., Hristov, V. V., Irwin, K., Kovac, J. M., Kuo, C. L., Lueker, M., Montroy, T., Nguyen, H. T., Ogburn, R. W., O'Brient, R., Orlando, A., Pryke, C., Reintsema, C., Ruhl, J. E., Schwarz, R., Sheehy, C., Stokes, S., Thompson, K. L., Teply, G., Tolan, J. E., Turner, A. D., Vieregg, A. G., Wilson, P., Wiebe, D., and Wong, C. L., "The Keck Array: A Multi Camera CMB Polarimeter at the South Pole," *Journal of Low Temperature Physics* **167**, 827–833 (June 2012).

[29] Staguhn, J. G., Kovács, A., Arendt, R. G., Benford, D. J., Decarli, R., Dwek, E., Fixsen, D. J., Hilton, G. C., Irwin, K. D., Jhabvala, C. A., Karim, A., Leclercq, S., Maher, S. F., Miller, T. M., Moseley, S. H., Sharp, E. H., Walter, F., and Wollack, E. J., "The GISMO Two-millimeter Deep Field in GOODS-N," *ApJ* **790**, 77 (July 2014).

[30] Ferkinhoff, C., Brisbin, D., Parshley, S., Nikola, T., Stacey, G. J., Schoenwald, J., Higdon, J. L., Higdon, S. J. U., Verma, A., Riechers, D., Hailey-Dunsheath, S., Menten, K. M., Güsten, R., Weiß, A., Irwin, K., Cho, H. M., Niemack, M., Halpern, M., Amiri, M., Hasselfield, M., Wiebe, D. V., Ade, P. A. R., and Tucker, C. E., "The Second-generation z (Redshift) and Early Universe Spectrometer. I. First-light Observation of a Highly Lensed Local-ulirg Analog at High-z," *ApJ* **780**, 142 (Jan. 2014).

[31] Gualtieri, R., Filippini, J. P., Ade, P. A. R., Amiri, M., Benton, S. J., Bergman, A. S., Bihary, R., Bock, J. J., Bond, J. R., Bryan, S. A., Chiang, H. C., Contaldi, C. R., Doré, O., Duivenvoorden, A. J., Eriksen, H. K., Farhang, M., Fissel, L. M., Fraisse, A. A., Freese, K., Galloway, M., Gambrel, A. E., Gandilo, N. N., Ganga, K., Gramillano, R. V., Gudmundsson, J. E., Halpern, M., Hartley, J., Hasselfield, M., Hilton, G., Holmes, W., Hristov, V. V., Huang, Z., Irwin, K. D., Jones, W. C., Kuo, C. L., Kermish, Z. D., Li, S., Mason, P. V., Megerian, K., Moncelsi, L., Morford, T. A., Nagy, J. M., Netterfield, C. B., Nolta, M., Osherson, B., Padilla, I. L., Racine, B., Rahlin, A. S., Reintsema, C., Ruhl, J. E., Runyan, M. C., Ruud, T. M., Shariff, J. A., Soler, J. D., Song, X., Trangsrud, A., Tucker, C., Tucker, R. S., Turner, A. D., van der List, J. F., Weber, A. C., Wehus, I. K., Wiebe, D. V., and Young, E. Y., "SPIDER: CMB polarimetry from the edge of space," *ArXiv e-prints* (Nov. 2017).

[32] Beyer, A. D., Kenyon, M. E., Echternach, P. M., Chui, T., Eom, B.-H., Day, P. K., Bock, J. J., Holmes, W. A., and Bradford, C. M., "Ultra-sensitive Transition-Edge Sensors for the Background Limited Infrared/Sub-mm Spectrograph (BLISS)," *Journal of Low Temperature Physics* , 143 (Dec. 2011).

[33] Day, P. K., LeDuc, H. G., Mazin, B. A., Vayonakis, A., and Zmuidzinas, J., "A broadband superconducting detector suitable for use in large arrays," *Nature* **425**, 817–821 (Oct. 2003).

[34] Maloney, P. R., Czakon, N. G., Day, P. K., Downes, T. P., Duan, R., Gao, J., Glenn, J., Golwala, S. R., Hollister, M. I., Leduc, H. G., Mazin, B. A., McHugh, S. G., Noroozian, O., Nguyen, H. T., Sayers, J., Schlaerth, J. A., Siegel, S., Vaillancourt, J. E., Vayonakis, A., Wilson, P., and Zmuidzinas, J., "MUSIC for sub/millimeter astrophysics," in [*Society of Photo-Optical Instrumentation Engineers (SPIE) Conference Series*], *Society of Photo-Optical Instrumentation Engineers (SPIE) Conference Series* **7741** (July 2010).

[35] Mazin, B. A., O'Brien, K., McHugh, S., Bumble, B., Moore, D., Golwala, S., and Zmuidzinas, J., "AR-CHONS: a highly multiplexed superconducting optical to near-IR camera," in [*Society of Photo-Optical Instrumentation Engineers (SPIE) Conference Series*], *Society of Photo-Optical Instrumentation Engineers (SPIE) Conference Series* **7735** (July 2010).

[36] Monfardini, A., Benoit, A., Bideaud, A., Swenson, L., Cruciani, A., Camus, P., Hoffmann, C., Désert, F. X., Doyle, S., Ade, P., Mauskopf, P., Tucker, C., Roesch, M., Leclercq, S., Schuster, K. F., Endo, A., Baryshev, A., Baselmans, J. J. A., Ferrari, L., Yates, S. J. C., Bourrion, O., Macias-Perez, J., Vescovi, C., Calvo, M., and Giordano, C., "A Dual-band Millimeter-wave Kinetic Inductance Camera for the IRAM 30 m Telescope," *ApJS* **194**, 24–+ (June 2011).

[37] Swenson, L. J., Day, P. K., Dowell, C. D., Eom, B. H., Hollister, M. I., Jarnot, R., Kovács, A., Leduc, H. G., McKenney, C. M., Monroe, R., Mroczkowski, T., Nguyen, H. T., and Zmuidzinas, J., "MAKO: a pathfinder instrument for on-sky demonstration of low-cost 350 micron imaging arrays," in [*Society of Photo-Optical Instrumentation Engineers (SPIE) Conference Series*], *Society of Photo-Optical Instrumentation Engineers (SPIE) Conference Series* **8452**, 0 (Sept. 2012).

[38] Adam, R., Adane, A., Ade, P. A. R., André, P., Andrianasolo, A., Aussel, H., Beelen, A., Benoît, A., Bideaud, A., Billot, N., Bourrion, O., Bracco, A., Calvo, M., Catalano, A., Coiffard, G., Comis, B., De Petris, M., Désert, F. X., Doyle, S., Driessen, E. F. C., Evans, R., Goupy, J., Kramer, C., Lagache, G., Leclercq, S., Leggeri, J. P., Lestrade, J. F., Macías-Pérez, J. F., Mauskopf, P., Mayet, F., Maury, A., Monfardini, A., Navarro, S., Pascale, E., Perotto, L., Pisano, G., Ponthieu, N., Revéret, V., Rigby, A., Ritacco, A., Romero, C., Roussel, H., Ruppin, F., Schuster, K., Sievers, A., Triqueneaux, S., Tucker, C., and Zylka, R., "The NIKA2 large-field-of-view millimetre continuum camera for the 30 m IRAM telescope," *A&A* **609**, A115 (Jan. 2018).

[39] Austermann, J. E., Beall, J. A., Bryan, S. A., Dober, B., Gao, J., Hilton, G., Hubmayr, J., Mauskopf, P., McKenney, C. M., Simon, S. M., Ullom, J. N., Vissers, M. R., and Wilson, G. W., "Millimeter-Wave Polarimeters Using Kinetic Inductance Detectors for TolTEC and Beyond," *Journal of Low Temperature Physics* (May 2018).

[40] Galitzki, N., Ade, P., Angilè, F. E., Ashton, P., Austermann, J., Billings, T., Che, G., Cho, H.-M., Davis, K., Devlin, M., Dicker, S., Dober, B. J., Fissel, L. M., Fukui, Y., Gao, J., Gordon, S., Groppi, C. E., Hillbrand, S., Hilton, G. C., Hubmayr, J., Irwin, K. D., Klein, J., Li, D., Li, Z.-Y., Lourie, N. P., Lowe, I., Mani, H., Martin, P. G., Mauskopf, P., McKenney, C., Nati, F., Novak, G., Pascale, E., Pisano, G., Santos, F. P., Scott, D., Sinclair, A., Soler, J. D., Tucker, C., Underhill, M., Vissers, M., and Williams, P., "Instrumental performance and results from testing of the BLAST-TNG receiver, submillimeter optics, and MKID detector arrays," in [*Millimeter, Submillimeter, and Far-Infrared Detectors and Instrumentation for Astronomy VIII*], *Proc. of the SPIE* **9914**, 99140J (July 2016).

[41] Baselmans, J. J. A., Bueno, J., Yates, S. J. C., Yurduseven, O., Llombart, N., Karatsu, K., Baryshev, A. M., Ferrari, L., Endo, A., Thoen, D. J., de Visser, P. J., Janssen, R. M. J., Murugesan, V., Driessen, E. F. C., Coiffard, G., Martin-Pintado, J., Hargrave, P., and Griffin, M., "A kilo-pixel imaging system for future space based far-infrared observatories using microwave kinetic inductance detectors," *A&A* **601**, A89 (May 2017).

[42] Echternach, P. M., Stone, K. J., Bradford, C. M., Day, P. K., Wilson, D. W., Megerian, K. G., Llombart, N., and Bueno, J., "Photon shot noise limited detection of terahertz radiation using a quantum capacitance detector," *Applied Physics Letters* **103**, 053510 (July 2013).

[43] Hailey-Dunsheath, S., Barlis, A. C. M., Aguirre, J. E., Bradford, C. M., Redford, J. G., Billings, T. S., LeDuc, H. G., McKenney, C. M., and Hollister, M. I., "Development of Aluminum LEKIDs for Balloon-Borne Far-IR Spectroscopy," *Journal of Low Temperature Physics* (Apr. 2018).

[44] Leduc, H. G., Bumble, B., Day, P. K., Eom, B. H., Gao, J., Golwala, S., Mazin, B. A., McHugh, S., Merrill, A., Moore, D. C., Noroozian, O., Turner, A. D., and Zmuidzinas, J., "Titanium nitride films for ultrasensitive microresonator detectors," *APPLIED PHYSICS LETTERS* **97** (SEP 6 2010).

[45] Duan, R., McHugh, S., Serfass, B., Mazin, B. A., Merrill, A., Golwala, S. R., Downes, T. P., Czakon, N. G., Day, P. K., Gao, J., Glenn, J., Hollister, M. I., Leduc, H. G., Maloney, P. R., Noroozian, O., Nguyen, H. T., Sayers, J., Schlaerth, J. A., Siegel, S., Vaillancourt, J. E., Vayonakis, A., Wilson, P. R., and Zmuidzinas, J., "An open-source readout for MKIDs," in [*Society of Photo-Optical Instrumentation Engineers (SPIE) Conference Series*], *Society of Photo-Optical Instrumentation Engineers (SPIE) Conference Series* **7741** (July 2010).

[46] Gordon, S., Dober, B., Sinclair, A., Rowe, S., Bryan, S., Mauskopf, P., Austermann, J., Devlin, M., Dicker, S., Gao, J., Hilton, G. C., Hubmayr, J., Jones, G., Klein, J., Lourie, N. P., McKenney, C., Nati, F., Soler, J. D., Strader, M., and Vissers, M., "An Open Source, FPGA-Based LeKID Readout for BLAST-TNG: Pre-Flight Results," *Journal of Astronomical Instrumentation* **5**, 1641003 (Mar. 2016).

[47] Dober, B., Becker, D. T., Bennett, D. A., Bryan, S. A., Duff, S. M., Gard, J. D., Hays-Wehle, J. P., Hilton, G. C., Hubmayr, J., Mates, J. A. B., Reintsema, C. D., Vale, L. R., and Ullom, J. N., "Microwave SQUID multiplexer demonstration for cosmic microwave background imagers," *Applied Physics Letters* **111**, 243510 (Dec. 2017).

[48] Kernasovskiy, S. A., Kuenstner, S. E., Karpel, E., Ahmed, Z., Van Winkle, D. D., Smith, S., Dusatko, J., Frisch, J. C., Chaudhuri, S., Cho, H. M., Dober, B. J., Henderson, S. W., Hilton, G. C., Hubmayr, J., Irwin, K. D., Kuo, C. L., Li, D., Mates, J. A. B., Nasr, M., Tantawi, S., Ullom, J., Vale, L., and Young, B., "SLAC Microresonator Radio Frequency (SMuRF) Electronics for Read Out of Frequency-Division-Multiplexed Cryogenic Sensors," *ArXiv e-prints* (May 2018).

[49] Hsiao, F., Tang, A., Kim, Y., Drouin, B., Chattopadhyay, G., and Chang, M. C. F., "A 2.2 gs/s 188mw spectrometer processor in 65nm cmos for supporting low-power thz planetary instruments," in [*2015 IEEE Custom Integrated Circuits Conference (CICC)*], 1–3 (Sept 2015).

[50] Zhang, Y., Kim, Y., Tang, A., Kawamura, J., Reck, T., and Chang, M. C. F., "A 2.6gs/s spectrometer system in 65nm cmos for spaceborne telescopic sensing," in [*2018 IEEE International Symposium on Circuits and Systems (ISCAS)*], 1–4 (May 2018).